Pressure-induced phase transition and increase of oxygen-iodine coordination in magnesium iodate

A. Liang,[1] R. Turnbull,[1] C. Popescu,[2] F. J. Manjón,[3] E. Bandiello,[1] P. Rodriguez-Hernandez,[4] A. Muñoz,[4] I. Yousef,[2] Z. Hebboul,[5] and D. Errandonea[1,*]

[1]*Departamento de Física Aplicada-ICMUV-MALTA Consolider Team, Universitat de València, c/Dr. Moliner 50, 46100 Burjassot, Valencia, Spain*

[2]*CELLS-ALBA Synchrotron Light Facility, Cerdanyola, 08290 Barcelona, Spain*

[3]*Instituto de Diseño para la Fabricación y Producción Automatizada, MALTA Consolider Team, Universitat Politècnica de València, Camí de Vera s/n, 46022 València, Spain*

[4]*Departamento de Física and Instituto de Materiales y Nanotecnología, MALTA Consolider Team, Universidad de La Laguna, 38206 La Laguna, Tenerife, Spain*

[5]*Laboratoire Physico-Chimie des Matériaux (LPCM), University Amar Telidji of Laghouat, BP 37G, Ghardaïa Road, Laghouat 03000, Algeria*

(Received 9 December 2021; revised 12 January 2022; accepted 8 February 2022; published 17 February 2022)

The structural and vibrational behavior of $Mg(IO_3)_2$ under compression has been investigated via a combination of high-pressure (HP) synchrotron x-ray diffraction (XRD), Raman scattering, and infrared spectroscopy experiments as well as first-principles *ab initio* calculations. In this paper, we reveal that $Mg(IO_3)_2$ undergoes a pressure-induced phase transition between 7.5 and 9.7 GPa at ambient temperature from a monoclinic (space group $P2_1$) to a trigonal (space group $P3$) structure. $Mg(IO_3)_2$ also exhibits the gradual formation of additional bonds between iodine and oxygen atoms in neighboring IO_3^- units with increasing pressure, thereby increasing the oxygen-iodine coordination from 3 to 6. The bond formation under compression is a consequence of the existence of lone electron pairs on the iodine cation. To accommodate the additional bonds, the I–O bonds within the original $[IO_3]^-$ trigonal pyramids increase in length under increasing compression. The appearance of additional Raman modes at 7.7 GPa and infrared modes at 9.6 GPa supports the phase transition observed in XRD experiments. Interestingly, the lengthening of I–O bonds causes a softening of several Raman modes under compression. We provide the crystal structure of the HP phase, the pressure-volume equations of state for both low- and HP phases, and the symmetry assignment of the Raman- and infrared-active modes of both phases.

DOI: 10.1103/PhysRevB.105.054105

I. INTRODUCTION

Metal iodates have recently attracted great interest in materials science, and they have been synthesized with a range of metal cation atoms, including alkali metals, alkaline-earth metals, transition metals, posttransition metals, and lanthanide elements. The properties of metal iodates, particularly their crystal structure, electronic structure, and second harmonic generation (SHG), have been well studied at ambient pressure [1–8]. Such research is significantly motivated by the search for a generation of high-performance nonlinear optical (NLO) materials and their potential application in photonic technologies. Due to the existence of a lone electron pair (LEP) on the I^{5+} cation, both the metal cation and the iodine cations are centered in asymmetric oxygen environments. The presence of such asymmetric units enhances the polarization effect in the noncentrosymmetric crystal structure of metal iodates, favoring a large SHG response [9,10]. By manipulating the direction of the polarization from the asymmetric coordination polyhedra, it is possible to produce polar materials with very large SHG responses. For instance, by introducing Nb^{5+} cations in metal iodates, Sun *et al.* [3] successfully synthesized $BaNbO(IO_3)_5$, which has a SHG response 14 times larger than that of the currently widely used NLO materials, i.e., potassium dihydrogen phosphate (KH_2PO_4), usually known as KDP. Moreover, metal iodates usually exhibit transparency in a wide wavelength region [11,12], high optical-damage thresholds, and high thermal stability [5,6,13], which make them the choice for the next generation of NLO materials.

Since the crystal structure plays a significant role in the SHG performance and electronic structure of metal iodates [14], one important question about them is how stable they are under external stimuli, particularly under stress and compression. In this context, it is important to investigate the behavior of magnesium iodate under compression. Moreover, pressure is an ideal external parameter to modify the crystal and electronic structure of $Mg(IO_3)_2$. Pressure allows the shortening of interatomic distances and consequent modification of interatomic interactions. Therefore, high-pressure (HP) results will help to improve the understanding of the main physical properties of $Mg(IO_3)_2$ and other iodates. They will allow us to obtain a deeper understanding of the role played by bonding and iodine LEPs [15], which could lead to unusual behaviors at HP [14,16–19].

The crystal structure of $Mg(IO_3)_2$ at ambient conditions was reported by Liang *et al.* [20] based on powder x-ray

*daniel.errandonea@uv.es

diffraction (XRD). According to these results, it belongs to the hexagonal space group $P6_3$. The reported unit cell parameters are $a = 5.4777$ Å and $c = 5.1282$ Å. This structure is isomorphic to that of α-$LiIO_3$, but the Mg atoms are located at the *2a* Wyckoff position in a 0.5 partial occupation. Recently, Phanon *et al.* [21] have reported that the crystal structure of $Mg(IO_3)_2$ is better described by a pseudohexagonal structure of monoclinic symmetry (space group $P2_1$) with similar lattice parameters: $a = 10.952$ Å, $b = 5.117$ Å, $c = 10.959$ Å, and $\beta = 120.01°$. In this structure, all atomic positions are fully occupied. Despite this disagreement in the literature, it is clear that the crystal structure of $Mg(IO_3)_2$ is formed by asymmetric MgO_6 octahedral units, which are each connected to six trigonal IO_3 pyramids, via the oxygen atoms at the octahedral vertices. This structure is qualitatively like that of $Zn(IO_3)_2$, $Co(IO_3)_2$, and other metal iodates. The framework of interconnected octahedra and trigonal pyramids makes these iodates very anisotropic and compressible [16,17]. Additionally, HP Raman scattering (RS) and Fourier transform infrared (FTIR) spectroscopies have shown soft high-frequency phonons and phase transitions at relative low pressures (LPs; $P < 10$ GPa) [16–18].

In this paper, we report a combined experimental and theoretical study of $Mg(IO_3)_2$ under compression. HP-XRD, HP-RS, and HP-FTIR measurements have been combined with density functional theory (DFT) calculations to systematically investigate the pressure-induced structural evolution, the stereochemically active LEP of I^{5+}, and the atomic vibrations of $Mg(IO_3)_2$. Here, we present evidence of a pressure-induced monoclinic-to-trigonal phase transition between 7.5 and 9.7 GPa, which has been confirmed by each of the four diagnostics used. The detailed crystal structural information and vibrational behavior for both the LP and HP phases are reported. We present evidence of a significant oxygen coordination increase in iodine at HP, which is explained by a shortening of the atomic distance between iodine, the oxygen in the second neighboring layer, and the decrease of the stereoactivity of the iodine LEP. We also show that this phenomenon causes the softening of several Raman modes and favors the occurrence of the phase transition.

II. METHODS

A. Sample preparation

Samples of $Mg(IO_3)_2$ were synthesized from an aqueous solution with a mixture of potassium iodate KIO_3 (99.5% purity, Sigma Aldrich) and anhydrous magnesium chloride $MgCl_2$ ($\geqslant$ 98% purity, Sigma Aldrich). Potassium iodate was first dissolved into concentrated nitric acid (2 mmol of KIO_3 in 10 mL of 7N nitric acid) and then added to an anhydrous magnesium chloride solution (1 mmol in 10 mL of 7N nitric acid). After being stirred thoroughly, the reaction mixture was slowly evaporated and maintained at 60 °C for a few days.

B. HP-XRD measurements

A membrane-type diamond anvil cell (DAC), with diamond culets of 400 μm, was used to generate the HP conditions. A stainless-steel gasket was first pre-indented to 40 μm in thickness, and a 180-μm-diameter hole was drilled to serve as the sample chamber. Pressure was measured using the equation of state (EOS) of copper [22] and a 16:3:1 methanol : ethanol : water mixture (MEW) was used as the pressure transmitting medium (PTM) [23].

In situ angle-dispersive powder HP-XRD data were collected at the BL04-MSPD beamline of synchrotron ALBA-CELLS [24]. The monochromatic x-ray beam with a wavelength of 0.4642 Å was focused on a 20 × 20 μm spot (full width at half maximum). The diffraction data were recorded with a Rayonix SX165 CCD image plate, high purity LaB_6 powder was used as the standard for sample-to-detector distance calibration, and the powder HP-XRD patterns were integrated by using the DIOPTAS program to obtain a two-dimensional (2D) XRD pattern [25]. The FULLPROF program was used to analyze (Rietveld refinement) the 2D XRD patterns [26].

C. HP-RS measurements

In the HP-RS experiment, a membrane-type DAC with the diamond culets of 500 μm was used to generate the HP conditions. A stainless-steel gasket was pre-indented to a thickness of 40 μm, and a 250-μm-diameter hole was drilled in the gasket to be used as the sample chamber. The PTM used in HP-RS experiment is the same as what we used in HP-XRD (16:3:1 MEW), and a ruby sphere was loaded, together with the sample and PTM, to determine the pressure by using the ruby fluorescence method [27]. Measurements were carried out in a backscattering geometry employing a He/Ne laser (632.8 nm) light source and a HORIBA Jobin Yvon LabRAM HR UV microspectrometer. Signal was recorded with a thermoelectrically cooled multichannel CCD detector, and the spectral resolution is better than 2 cm^{-1}. Before the HP-RS experiment, the setup was calibrated by using the He plasma lines for pressure calibration and with the Si Raman-active mode for RS measurements.

D. HP-FTIR measurements

For HP-FTIR measurements, $Mg(IO_3)_2$ powder was pressed into compact 10-μm-thick platelets before being loaded in a DAC equipped with IIAC diamonds with culets of 300 μm. Cesium iodide CsI was used as the solid PTM since it is transparent to a wide frequency range of IR light [28]. Notice that this PTM and MEW becomes nonhydrostatic in the pressure range of the experiments. However, we found a remarkable agreement between the three types of experiments and DFT simulations (which are done under fully hydrostatic conditions) suggesting that the influence of nonhydrostatic effect in the behavior of $Mg(IO_3)_2$ up to 24 GPa is not as relevant as in other materials [29]. A stainless-steel gasket, which was pre-indented to a thickness of 40 μm and drilled with a hole in the center of 150 μm, was used as the sample chamber. The ruby fluorescence method was employed for the pressure calibration [27]. HP-FTIR microspectroscopy measurements in transmission mode were conducted at the MIRAS beamline of the ALBA-CELLS synchrotron [30]. The size of the masking aperture is 50 × 50 cm^2, and the beam current was 250 mA. The measurement was performed

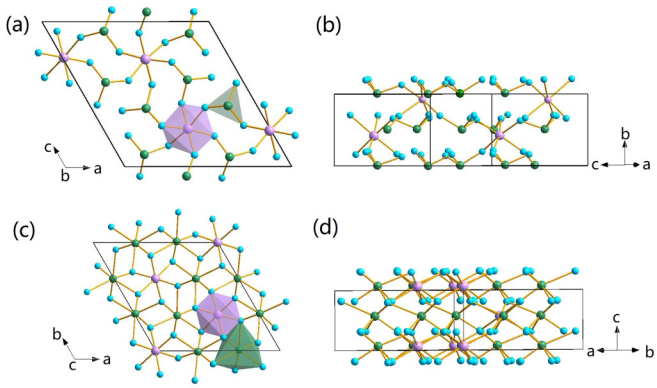

FIG. 1. Crystal structure of the low-pressure (LP) phase of $Mg(IO_3)_2$ (space group $P2_1$) (a) along the b axis and (b) perpendicular to the b axis. Crystal structure of the high-pressure (HP) phase of $Mg(IO_3)_2$ (space group $P3$): (c) along the c axis and (d) perpendicular to the c axis. Purple circles represent Mg atoms while green and sky-blue circles represent I and O atoms, respectively. Bonds between cations and oxygen are also shown. Polyhedral coordination is shown in (a) and (c).

in a Hyperion 3000 microscope coupled to a Vertex 70 spectrometer. The data were collected by a He-cooled bolometer detector, and the resolution of the spectra was $4\,cm^{-1}$. The used setup has a wave number cutoff of $700\,cm^{-1}$. More experimental details can be found in our previous works [17,31].

E. First-principles calculations

The *ab initio* simulations were performed within the framework of DFT [32] using the Vienna *Ab initio* Simulation Package [33] with the projector augmented-wave pseudopotentials [34,35]. Computer simulations were carried out using the primitive cell of the crystal structures. The plane-wave kinetic energy cutoff was large enough 530 eV to ensure highly converged results. Benchmark calculations showing the convergence of the simulation results with respect to the cutoff energy are provided in the Supplemental Material, Fig. S1 [36]. The Monkhorst-Pack scheme was employed for the Brillouin zone (BZ) integrations with a $6 \times 4 \times 6$ ($6 \times 6 \times 4$) grid of k-special points [37] for the LP (HP) phase. Exchange-correlation energy was described using the generalized gradient approximation with the Armiento and Mattsson AM05 [38,39] prescription.

The unit cell parameters and the atomic positions were fully optimized to obtain, at selected volumes, the relaxed structures requiring that the forces on the atoms were <0.003 ev/Å and that the deviations of the stress tensors from a diagonal hydrostatic form <0.1 GPa. The simulations provide a set of volume, energy, and pressure (from the stress tensor), which are fitted with a Birch-Murnaghan EOS to obtain the theoretical equilibrium volume, the bulk modulus, and its pressure derivatives.

Lattice-dynamic calculations of the phonon modes were carried out at the zone center (Γ point) of the BZ with the direct force-constant approach [40]. These calculations provide not only the frequency of the normal modes but also their symmetry and their polarization vectors. This allows us to identify the irreducible representations and the character of the phonon modes at the Γ point.

TABLE I. Crystal structure information of the LP and HP phases obtained from the Rietveld refinement of the XRD respectively at ambient pressure and 10.5 GPa.

Atom	Wyckoff	x	y	z
Ambient pressure, space group $P2_1$, $a = 11.2563$ Å, $b = 5.0497$ Å, $c = 11.2128$ Å, $\beta = 119.8256^\circ$				
Mg_1	$2a$	0.508	0.426	0.319
Mg_2	$2a$	−0.008	0.920	0.402
I_1	$2a$	0.159	0.503	0.097
I_2	$2a$	0.327	0.008	0.401
I_3	$2a$	0.826	0.014	0.419
I_4	$2a$	0.661	0.510	0.066
O_1	$2a$	0.464	0.610	0.170
O_2	$2a$	−0.086	1.017	−0.212
O_3	$2a$	0.261	0.658	0.306
O_4	$2a$	0.390	0.122	0.211
O_5	$2a$	0.103	0.245	0.420
O_6	$2a$	0.415	0.188	0.554
O_7	$2a$	0.547	0.174	0.325
O_8	$2a$	1.240	−0.421	0.737
O_9	$2a$	1.047	0.178	0.239
O_{10}	$2a$	0.707	0.721	0.209
O_{11}	$2a$	0.894	0.745	0.132
O_{12}	$2a$	0.503	1.238	−0.213
$P = 10.5$ GPa, space group $P3$, $a = 9.8336$ Å, $c = 3.8652$ Å				
Mg_1	$1b$	0.333	0.667	0.628
Mg_2	$1c$	0.667	0.333	0.128
Mg_3	$1a$	0.000	0.000	1.000
I_1	$3d$	0.334	0.977	0.095
I_2	$3d$	0.676	0.019	0.604
O_1	$3d$	0.984	0.053	0.680
O_2	$3d$	0.110	0.933	0.926
O_3	$3d$	0.577	0.127	0.224
O_4	$3d$	0.540	0.846	0.719
O_5	$3d$	0.197	0.720	0.301
O_6	$3d$	0.809	0.290	0.859

III. RESULTS AND DISCUSSION

A. HP-XRD measurements

1. Pressure-induced phase transition

Based upon Rietveld refinements of the XRD pattern of $Mg(IO_3)_2$ at ambient pressures (Supplemental Material, Fig. S2 [36]), we ruled out the hexagonal crystal structure proposed by Liang *et al.* [20], which fails to describe all of the diffraction peaks. Instead, we found that the XRD pattern of the LP phase corresponds to the monoclinic structure (space group $P2_1$) reported by Phanon *et al.* [21]. The crystal structure is shown in Figs. 1(a) and 1(b). Structural information on the crystal structure of the LP phase is given in Table I. When viewed along the b axis, the crystal structure consists of two asymmetric polyhedral units. One is the distorted MgO_6 octahedron with an off-centered Mg atom. The other is the IO_3 trigonal pyramid. This is a polar molecule, where the

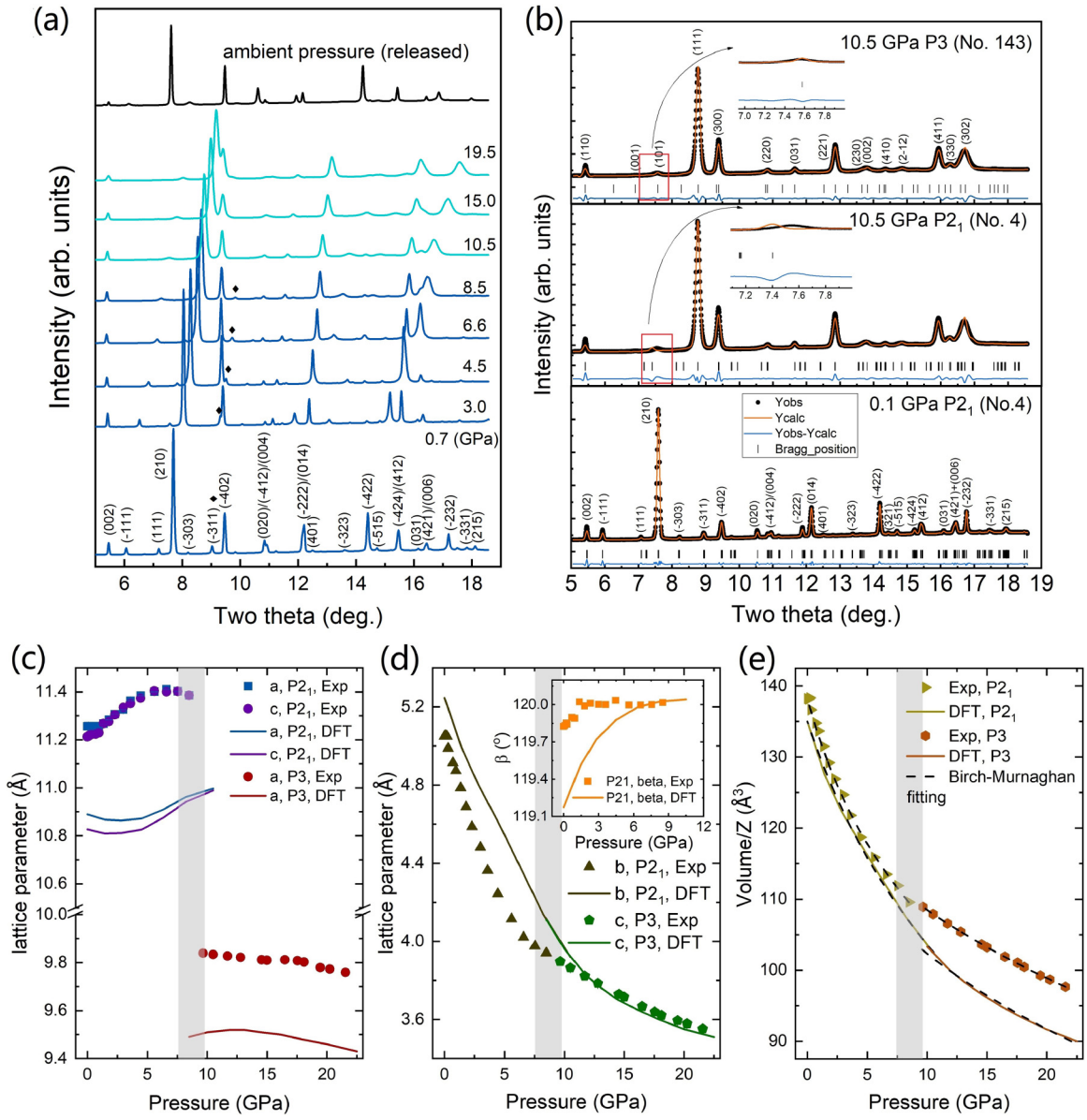

FIG. 2. Selections of high-pressure x-ray diffraction (HP-XRD) patterns. (a) Representative HP-XRD patterns of $Mg(IO_3)_2$. The XRD patterns of different phase are shown in different colors. Pressures are given in the right of each pattern in gigapascals. The black diamond shows the evolution of peak $(\bar{3}11)$ under compression. (b) Rietveld refinements at 0.1 and 10.5 GPa. For the HP phase, we show refinements with the low-pressure (LP) and HP crystal structures to support the assignment of the trigonal structure. Black dots show experimental data, orange lines are the refined patterns, ticks show the positions of diffraction peaks, and blue lines show the residuals. (c) and (d) Experimental and calculated pressure dependence of the different lattice parameters which are indicated in the figure. In (d), the inset is the pressure dependence of the monoclinic angle β. (e) Unit cell volume per formula unit as a function of pressure obtained from experiments and calculations. In (c)–(e), the phase transition region is marked as a grey rectangle.

three O atoms form the base of the pyramid, the I atom is located at the vertex, and the nonbonding LEP of the I^{5+} ion points in the opposite direction to the base of the pyramid. In Figs. 1(a) and 1(b), each MgO_6 octahedron is surrounded by six IO_3 pyramids due to the sharing of one O atom and every two MgO_6 octahedral units were bridged by two IO_3 units. When viewed perpendicular to the *b* axis, the structure of $Mg(IO_3)_2$ can be described as a 2D crystal structure, where layers of IO_3 pyramids are linked by MgO_6 octahedra.

Representative HP-XRD spectra of $Mg(IO_3)_2$ are shown in Fig. 2(a). Rietveld refinements of the XRD patterns collected at 0.1 and 10.5 GPa are shown in Fig. 2(b). At pressures up to 8.5 GPa, XRD patterns can be well refined by the ambient-pressure monoclinic crystal structure (space group $P2_1$) [21]. This is illustrated by the Rietveld refinement at 0.1 GPa which is shown in Fig. 2(b) ($R_p = 9.23\%$ and $R_{wp} = 8.85\%$). Under compression, most diffraction peaks shift to higher angles because of the unit cell contraction, but many diffraction peaks evolved in a different way, an indication of anisotropic

TABLE II. EOS of $Mg(IO_3)_2$ as determined by experiment and theoretical calculation for LP and HP phases, respectively.

	LP phase ($Z = 4$)			HP phase ($Z = 3$)		
Data source	V_0/Z (Å^3)	B_0 (GPa)	$B_0^{'}$	V_0/Z(Å^3)	B_0 (GPa)	$B_0^{'}$
Experiment	138.2	22.2 (0.8)	4.2 (0.4)	123.2 (0.1)	63.6 (0.4)	3.3 (0.1)
Calculation	135.0	26.4 (0.8)	2.9 (0.2)	121.3 (1.5)	44.4 (2.4)	3.6 (0.4)

behavior. For instance, the peak (002) almost remains unchanged at HP up to the highest pressure in our experiment, but the strongest peak (210) shifts continuously to higher angles, merging with peak ($\bar{4}02$) at HP. There is no obvious evidence of a structural phase transition up to 9.7 GPa. Above this pressure, peak ($\bar{1}11$) exhibits a sudden change in its shift rate under compression from 8.5 to 9.7 GPa (Supplemental Material, Fig. S3 [36]). On top of that, peaks (111) and ($\bar{3}11$) disappear. These and other subtle changes in the XRD pattern suggest an increase of symmetry of the crystal structure >9.7 GPa. In fact, the $P2_1$ space group predicts reflections that are not present in the XRD patterns beyond 8.5 GPa, as noted in the Rietveld refinement at 10.5 GPa in Fig. 2(b). These facts indicate the occurrence of a phase transition that has been further confirmed by the HP-RS and HP-FTIR measurements and DFT calculations discussed later.

Indexing the XRD pattern measured at 10.5 GPa leads to hexagonal or trigonal structures for the HP phase of $Mg(IO_3)_2$. After several attempts, we successfully refined the XRD pattern at 10.5 GPa by adopting the trigonal space group $P3$. The obtained refinement ($R_p = 10.6\%$ and $R_{wp} = 10.1\%$) is shown in Fig. 2(b). The refined crystal structure parameters of the HP phase at 10.5 GPa are given in Table I. The crystal structure of the HP phase is shown in Figs. 1(c) and 1(d). When viewed along the c axis (which is equivalent to the b axis of the monoclinic structure), the HP phase shows MgO_6 octahedra surrounded by six distorted IO_6 octahedra (two O atoms are shared between each octahedron). In this context, the oxygen coordination of I increases from threefold in the LP phase to sixfold in the HP phase (if we chose 2.48 Å as the bonding limitation between iodine and oxygen atoms) [16,41]. When viewed perpendicular to the c axis, the HP phase of $Mg(IO_3)_2$ shows the transformation from the 2D layered structure of the LP phase to a three-dimensional structure. This is caused by the formation of extra bonds between iodine and oxygen atoms of the neighboring IO_3 layer. The I coordination change in the HP phase is discussed in detail later. We found that the pressure-induced structural phase transition in $Mg(IO_3)_2$ is reversible, as seen in the XRD collected after fully releasing pressure [top pattern in Fig. 2(a)]. More evidence of the reversibility can be found in the HP-RS and HP FTIR experiments later discussed.

2. Compressibility

From experiments and calculations, we determined the pressure dependence of the lattice parameters and unit cell volume of the LP and HP phases. Results are shown in Figs. 2(c) to 2(e). The agreement between the experimental and calculated lattice parameters reflects the reasonable description provided by *ab initio* calculations for the crystal structure behavior under compression. In the LP phase, the crystal structure exhibits an unusual expansion of the a and c axes, which gradually become equivalent. In contrast, according to experiments (calculations), the lattice parameter b shows a dramatic shrinkage from 5.1 Å (5.2 Å) at ambient pressure to 4.0 Å (4.4 Å) at 6.6 GPa. This implies a 21.6% (15.4%) reduction that contrasts with the much smaller changes of the other two axes (1.4 and 1.7%, respectively, for a and c according to experiment). Thus, the behavior of the crystal structure of the LP phase of $Mg(IO_3)_2$ is highly anisotropic under compression. The large compressibility along the b axis is a consequence of the layered characteristic of the crystal structure, which consists of layers stacked along to the b axis [see Fig. 1(b)] with a relatively large empty space between each layer due to the alignment of the iodine LEP along the b axis. Regarding the monoclinic angle of the LP phase, it increases from 119.8° at ambient pressure to ∼120° at 1.4 GPa in experiment, and after that, it becomes roughly constant within the experimental accuracy. Similar behavior is observed in the calculated monoclinic angle [see Fig. 2(d)]. Notice that, at 8.5 GPa, the unit cell parameters a and c are nearly identical, i.e., the crystal structure can be described as pseudohexagonal. Interestingly, >8.5 GPa, the phase transition to the trigonal phase takes place.

In the HP phase, both lattice parameters a and c are less sensitive to pressure than the unit cell parameters of the LP phase. For instance, the lattice parameter c of the HP phase, which corresponds to the b parameter of the LP phase, shows a reduction of 8.8% (11.4%) from 10 to 22 GPa according to experiments (calculations). This means that the compressibility of c in the HP phase is half that of the equivalent parameter of the LP phase. The fact that HP phase is less compressible than the LP phase also causes an increase of the bulk modulus, as can be seen in Table II, where we have summarized the zero-pressure volume (V_0), bulk modulus (B_0), and its pressure derivate ($B_0^{'}$) for both phases. Parameters in Table II were obtained from fitting the P-V data for both phases using a third-order Birch-Murnaghan EOS [42,43] with the EOSFIT7C-GUI software [44]. To better compare both phases, we have used the volume per formula unit in both Fig. 2(e) and Table II. The bulk moduli for the LP phase obtained from experiments and calculations, 22.2 ± 0.8 and 26.4 ± 0.8 GPa, respectively, are in good agreement and are like those of the LP phase of KIO_3 (24.3 GPa) [45] and $Zn(IO_3)_2$ (21.6 GPa) [16], slightly smaller than that of the LP phase of $Co(IO_3)_2$ (29.8 GPa) [17] and α-$LiIO_3$ (34 GPa) [46], and much smaller than that of the LP phase of $Fe(IO_3)_3$ (55 GPa) [19]. The bulk modulus of the HP phase is almost three times larger than that of LP phase in experiment. In addition, the bulk modulus of the HP phase in $Mg(IO_3)_2$ is close to that of the HP phase of

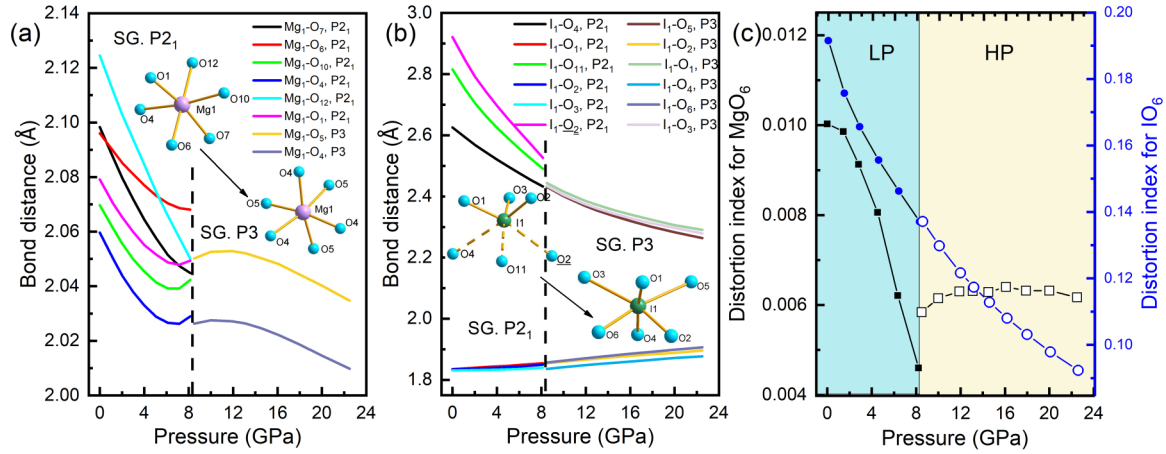

FIG. 3. Calculated pressure dependence of (a) Mg_1-O and (b) I_1-O bond distances. Polyhedral coordination is shown in the figure. The vertical dash line indicates the phase transition pressure. (c) Calculated distortion index of Mg_1O_6 (squares) and I_1O_6 (circles) octahedral extrapolated from the calculated structure by using the VESTA software program [50]. For a better comparison of the distortion index of the oxygen environment in iodine, we used the distortion index of IO_6 units for the whole pressure range.

$Co(IO_3)_2$ (70.8 GPa) [17] and the HP phase of $Fe(IO_3)_3$ (73 GPa) [19].

3. Oxygen coordination increase of iodine

In this section, we demonstrate the pressure-induced oxygen coordination increase of iodine. The calculated Mg-O and I-O bond distances as a function of pressure are shown in Figs. 3(a) and 3(b). In the LP phase, Mg atoms are bonded to six O atoms in six different Wyckoff positions. All six Mg-O bond lengths are different from each other, resulting in a distorted MgO_6 octahedron. On the other hand, the iodine atoms are only bonded to three O atoms; however, for a better comprehension of changes in iodine coordination, we will consider in our analysis IO_6 units by including the distances between the iodine atom and the three second nearest neighboring O atoms, which in the case of I1 are O4, O11, and the second nearest neighboring $\underline{O_2}$ [see the long I-O bonds in Fig. 3(b)]. Due to the large difference between the three short and the three long I-O bond distances, the distortion

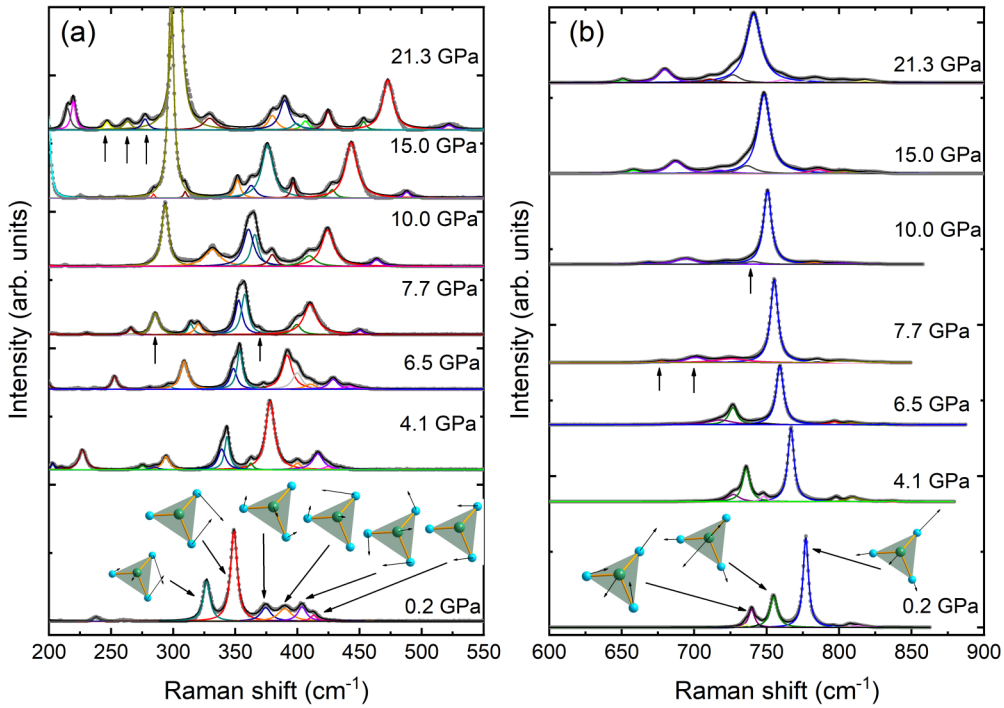

FIG. 4. Background-subtracted Raman spectra of $Mg(IO_3)_2$ at selected pressures in two different wave number ranges. Experimental results are shown in gray dots, and the fitting of Raman peaks via a Voigt profiles is shown with solid lines of different colors. The intensity axis of (a) is multiplied by a factor of 10 relative to (b) to show Raman-active peaks more clearly.

TABLE III. Frequency (ω), pressure coefficient ($d\omega/dP$), and Grüneisen parameters (γ) for different Raman-active modes of the LP phase. The pressure coefficients of each mode shown in this paper were extracted by fitting the Raman shift vs pressure plot in Fig. 5 with the quadratic function: $\omega = C + AP + BP^2$, where C, A, and B are constants, and P is pressure. The Grüneisen parameters were calculated by the expression $\gamma_0 = (B_0/\omega_0)(d\omega/dP)$, where B_0 is the bulk modulus we obtained from the HP-XRD data. For the sake of simplicity, we only listed the calculated modes that have been tentatively assigned to the modes observed in experiment. All calculated modes can be found in Table S1 in the Supplemental Material [36].

	Theory (ambient pressure, $B_0 = 26.4$ GPa)			Experiment (0.2 GPa, $B_0 = 22.2$ GPa)		
Modes	ω (cm^{-1})	$d\omega/dP$ (cm^{-1}/GPa)	γ	ω (cm^{-1})	$d\omega/dP$ (cm^{-1}/GPa)	γ
A	64.34	6.35	2.61	62	7.69	2.75
B	81.49	2.62	0.85	76	8.37	2.45
B	112.08	5.77	1.36	115	12.29	2.37
A	140.00	5.58	1.05	135	8.89	1.46
A	145.67	5.63	1.02	146	11.94	1.82
B	165.81	7.80	1.24	156	14.06	2.00
A	172.45	7.62	1.17	165	12.23	1.64
B	175.35	8.56	1.29	177	5.22	0.65
A	185.73	10.18	1.45	188	10.54	1.24
B	242.47	8.39	0.91	238	10.67	1.00
B	324.99	5.27	0.43	327	3.72	0.25
A	351.21	6.70	0.50	349	8.91	0.57
B	381.86	8.92	0.62	374	7.84	0.47
A	388.14	9.53	0.65	390	9.31	0.53
B	397.74	8.96	0.59	404	6.22	0.34
A	409.35	9.20	0.59	413	5.42	0.29
A	731.01	−3.78	−0.14	735	−3.85	−0.12
A	736.14	−4.92	−0.18	739	−2.80	−0.08
B	746.28	−3.84	−0.14	755	−5.78	−0.17
A	770.97	−3.58	−0.12	777	−2.21	−0.06
A	796.35	3.01	0.10	796	1.18	0.03
B	810.49	2.19	0.07	813	−1.27	−0.03

index of IO_6 units is ∼0.19 at ambient pressure [see Fig. 3(c)]. Under compression, the distortion index of MgO_6 and IO_6 units decreases, thus indicating the increase of the symmetry of the structure at HP.

In the HP phase, Mg is in three different Wyckoff positions, and each of them is bonded with six oxygen atoms in two different Wyckoff positions. Then there are only two types of Mg-O bonds in each MgO_6 octahedron, and the distortion index of this unit almost remains unchanged after the phase transition. On the other hand, both the short and long I-O bonds show a continuous change under compression in the HP phase, and the distortion index of the IO_6 units continuously decreases up to ∼24 GPa.

An interesting feature regarding the IO_6 units is the opposing evolution of the short and long I-O bond distances [see Fig. 3(b)]. The three short I-O bonds expand under compression in both the LP and HP phases, while the three long I-O bonds shrink. Moreover, if we choose 2.48 Å as the maxima bonding distance between I and O atoms [41,47], the iodine coordination gradually increases and becomes sixfold in the HP phase. Due to the existence of the iodine LEP, which will typically point out of the IO_3 layer [1,15], and the pressure-induced shortening of the long I-O bond distances, iodine will gradually bond with the oxygen in the neighboring IO_3 layer, which will be accompanied by the decrease of the stereoactivity of the LEP. Therefore, the three oxygen atoms in the trigonal IO_3 pyramid will be pushed away from iodine to accommodate the additional three incoming oxygen atoms. A similar increase of the I coordination to O atoms has also been reported in other metal iodates, like $Fe(IO_3)_3$ [18,19], $Zn(IO_3)_2$ [16], $Co(IO_3)_2$ [17], KIO_3 [48], and in 2D bismuth-based materials, like Bi_2O_2S [15]. As the new I-O bonds are formed and the Mg-O bond distance also shortens, the repulsive interaction between atoms becomes significant and resists the external compression. Eventually, the crystal structure of the HP phase becomes less compressible, and the bulk modulus in experiment ($B_0 = 63.6 \pm 0.4$ GPa) becomes three times higher than that of the LP phase.

B. HP-RS measurements

According to group theory, the LP phase (space group $P2_1$) has 54A + 54B modes at the BZ center. One A and two B modes are acoustic vibrations. The remaining 105 modes are optical modes, which are both Raman- and IR-active modes. On the other hand, the HP phase (space group $P3$) should have 27A + 27E vibrational modes at the BZ center. In this case, one A and one E modes are acoustic modes. Again, the remaining 52 modes are both Raman- and IR-active modes. It must be noted that, since all modes in both phases are both Raman- and IR-active, they are polar and can show a transverse optical−longitudinal optical (TO-LO) splitting. Therefore, up to double the number of modes can be observed in the spectra.

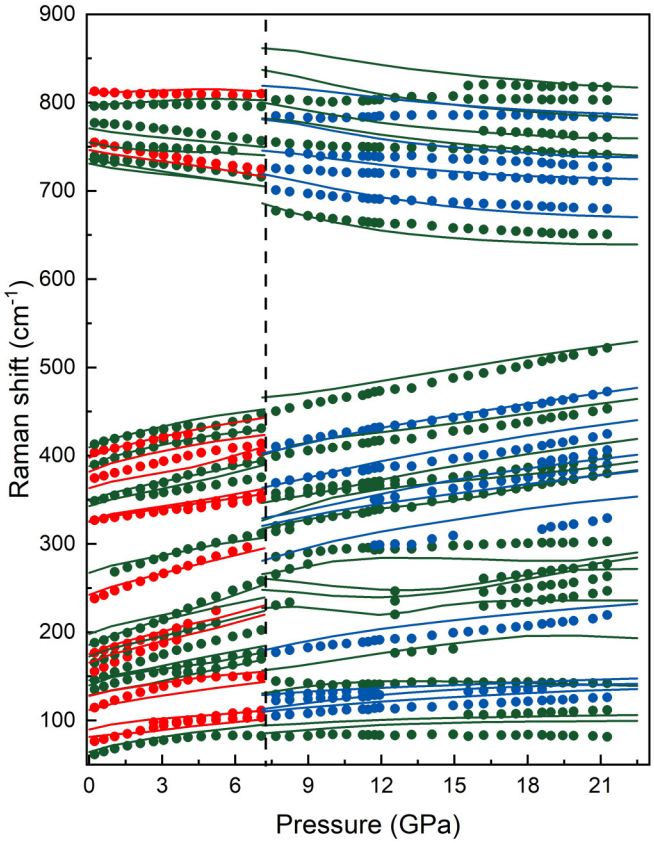

FIG. 5. Calculation (solid lines) and experiment (dots) determined pressure dependence of the Raman modes; the vertical dashed line indicates the phase transition pressure. For the low-pressure (LP) phase, A and B symmetry modes are shown in green and red, respectively. For the high-pressure (HP) phase, A and E symmetry modes are shown in green and blue, respectively. For the sake of simplicity, we only plotted the calculated modes which correlate to the experiment observed modes. The theoretical results of the HP phase at wave numbers $> 600\,\mathrm{cm}^{-1}$ have been upshifted by $70\,\mathrm{cm}^{-1}$ to match with the experimental results.

Raman spectra of $Mg(IO_3)_2$ at selected pressures are shown in two ranges: from 200 to $550\,\mathrm{cm}^{-1}$ [Fig. 4(a)] and from 600 to $900\,\mathrm{cm}^{-1}$ [Fig. 4(b)]. The entire range of the Raman spectra (from 10 to $1000\,\mathrm{cm}^{-1}$) at selected pressures can be found in the Supplemental Material, Fig. S4 and Table S1 [36]. We only present these two ranges in this paper because they provide the most interesting information regarding the HP behavior of $Mg(IO_3)_2$. The spectra are split into two different plots because of the intensity difference between the modes in the two ranges.

Near ambient pressure (0.2 GPa), a total of 22 Raman-active modes have been detected (see Table III). The symmetries of the different Raman-active modes have been assigned with the help of calculations because calculated frequencies show a rather good agreement with experimental ones. Moreover, the experimental pressure dependence of the frequencies of the Raman-active modes is well described by calculations (see Fig. 5). Seven modes are observed in the midfrequency range (200 to $550\,\mathrm{cm}^{-1}$) and six in the high-frequency range (600 to $900\,\mathrm{cm}^{-1}$).

Thanks to calculations, the atomic displacements associated with the observed Raman-active modes have been obtained. Raman-active modes of the midfrequency range are associated with the internal bending of $[IO_3]^-$ polyhedron, while modes of the high-frequency range are associated with the internal stretching of IO_3^- units. On the other hand, the modes $< 200\,\mathrm{cm}^{-1}$ are associated with the translational and rotational motions of iodate as a rigid unit. This result is like those previously found in other metal iodates, such as KIO_3 [48], $Mn(IO_3)_2$ [49], $Fe(IO_3)_3$ [18], $Zn(IO_3)_2$ [16], and $Co(IO_3)_2$ [17].

In the midfrequency range [Fig. 4(a)], the strongest mode near ambient pressure is $\sim 349\,\mathrm{cm}^{-1}$ and has been assigned to the I-O symmetric bending mode of the $[IO_3]^-$ unit. The modes at 374, 390, and $413\,\mathrm{cm}^{-1}$ are also assigned to the I-O symmetric bending modes, and the modes at 327 and $404\,\mathrm{cm}^{-1}$ are assigned to the I-O asymmetric bending modes of the $[IO_3]^-$ unit. All these modes of the midfrequency region stiffen under compression. Notably, the mode at $327\,\mathrm{cm}^{-1}$ splits beyond 4.1 GPa as a consequence of the different pressure dependence of two constituent modes which have almost the same frequency at 0.2 GPa (see Fig. 5).

Above 7.7 GPa, two additional Raman peaks appear [see arrows in Fig. 4(a)]. The intensity of these two peaks grows with increasing pressure. We consider these modes are an indication of the onset of a phase transition, which agrees with the results of HP-XRD. By using the same symmetry assignment provided by calculations, the Raman modes of the HP phase at 7.7 GPa and their vibration symmetry have been determined (see Tables IV and S2 in the Supplemental Material [36]). There are three Raman peaks that become more evident near 17 GPa at $\sim 250\,\mathrm{cm}^{-1}$, but we interpret that these modes are not an indication of any structural change since we consider that these modes are predicted by calculations for the HP phase. We consider that these modes already exist >7.7 GPa, but unfortunately, they are too weak to be accurately determined, so they are not included in Fig. 4. According to calculations, these modes have a nonlinear pressure dependence (see Fig. 5), with a softening from 7.5 to 12 GPa and then a subsequent hardening.

In the high-frequency range [Fig. 4(b)], the strongest Raman peak, which also is the strongest Raman peak of the spectrum, is located at $777\,\mathrm{cm}^{-1}$ at 0.2 GPa in LP phase. The frequency of this mode is comparable with that of the strongest mode of $Zn(IO_3)_2$ ($782\,\mathrm{cm}^{-1}$) [16], $Fe(IO_3)_3$ ($790\,\mathrm{cm}^{-1}$) [18], $Co(IO_3)_2$ ($765\,\mathrm{cm}^{-1}$) [17], $Mn(IO_3)_2$ ($774\,\mathrm{cm}^{-1}$) [49], and KIO_3 ($750\,\mathrm{cm}^{-1}$) [48]. This is reasonable since, in all the above-mentioned compounds, the strongest mode corresponds to the same internal I-O stretching vibration of the $[IO_3]^-$ unit. Thanks to calculations, we have assigned the modes at 735 and $755\,\mathrm{cm}^{-1}$ to the asymmetric I-O stretching modes of $[IO_3]^-$ and the mode at $777\,\mathrm{cm}^{-1}$ to the symmetric I-O stretching mode of $[IO_3]^-$. It is worth noting that the three modes soften under compression. At 7.7 GPa, we found three extra Raman peaks. They are marked by arrows in Fig. 4(b). In addition, there is an intensity drop of the mode $755\,\mathrm{cm}^{-1}$ (at 0.2 GPa), and the modes at frequencies $> 777\,\mathrm{cm}^{-1}$ disappear. The changes observed in the high-frequency range of the spectrum also support the occurrence of the phase transition we found in HP-XRD. Interestingly,

TABLE IV. Frequency (ω), pressure coefficient ($d\omega/dP$), and Grüneisen parameters (γ) for different Raman-active modes of the HP phase. More details can be found in the caption of Table III. All theoretical predicted modes at 8.5 GPa can found in Table S2 in Supplemental Material [36]. The miss of the pressure coefficient and Grüneisen parameters for the experimental mode at 231 cm^{-1} is due to insufficient data at HP.

	Theory (8.5 GPa, $B_0 = 44.4$ GPa)			Experiment (7.7 GPa, $B_0 = 63.6$ GPa)		
Modes	ω (cm^{-1})	$d\omega/dP$ (cm^{-1}/GPa)	γ	ω (cm^{-1})	$d\omega/dP$ (cm^{-1}/GPa)	γ
A	88.39	1.93	0.97	82	0.45	0.35
E	113.68	2.38	0.93	105	1.72	1.04
E	118.12	3.40	1.28	123	1.56	0.81
E	131.76	1.59	0.53	130	0.82	0.40
A	136.93	2.35	0.76	144	0.07	0.03
E	187.53	4.95	1.17	177	2.70	0.97
A	228.93	0.06	0.01	231	×	×
E	271.82	2.32	0.38	286	4.20	0.93
A	325.46	4.08	0.56	320	4.05	0.81
A	340.00	6.22	0.81	353	2.81	0.51
A	353.44	5.79	0.73	358	3.72	0.66
E	371.86	6.33	0.76	369	3.09	0.53
A	412.55	4.62	0.50	399	3.46	0.55
E	411.22	5.92	0.64	410	4.19	0.65
A	469.89	4.30	0.41	451	4.66	0.66
A	624.40	−6.21	−0.44	678	−3.20	−0.30
E	661.56	−5.81	−0.39	701	−2.16	−0.20
E	692.15	−3.77	−0.24	726	−0.98	−0.09
A	728.70	−4.30	−0.26	755	−0.62	−0.05
E	766.70	−3.26	−0.19	785	0.71	0.06
A	780.14	−6.10	−0.35	803	0.88	0.07

in both the LP and HP phases, several high-frequency modes show a soft behavior (see Fig. 5). As we have previously demonstrated in $Zn(IO_3)_2$ [16], for the internal I-O stretching modes of $[IO_3]^-$, $\omega^{-2/3}$ shows a linear relationship with the average I-O bond. Therefore, it is reasonable to conclude that the soft behavior of the Raman modes in $Mg(IO_3)_2$ is caused by the enlargement of the three short I-O bonds under compression to accommodate the three additional oxygen atoms. This observation agrees with the results shown at the bottom of Fig. 3(b), and it is expected that the increase of the short I-O

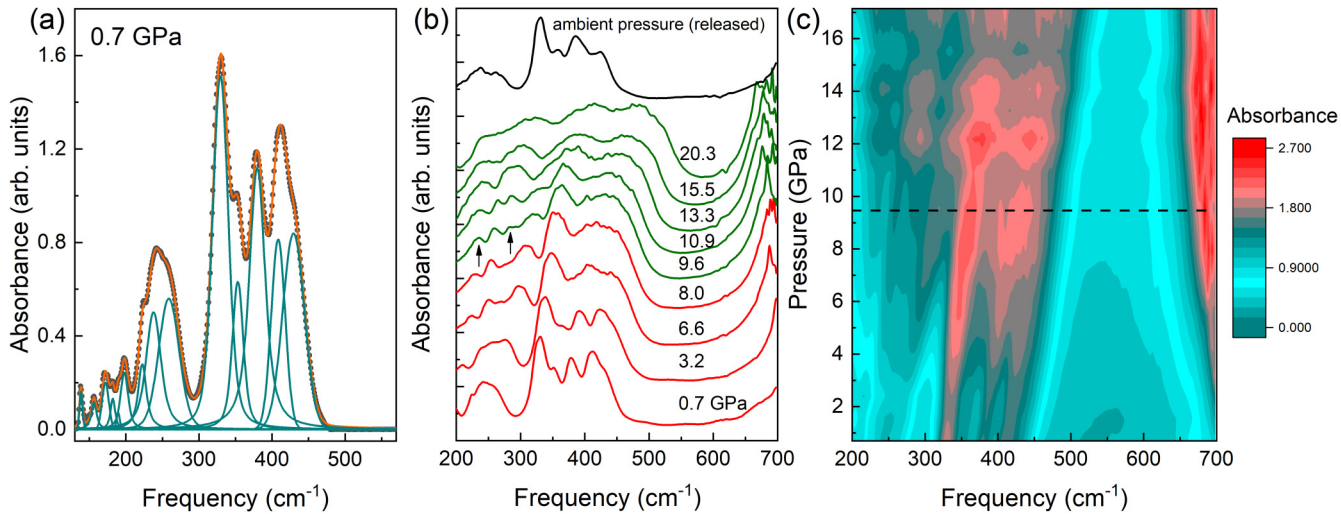

FIG. 6. Infrared (IR) spectra of $Mg(IO_3)_2$ at selected pressures. (a) Background-subtracted IR spectra at the lowest pressure in our experiment (0.7 GPa); experimental data are shown by gray dots, the fitting of the experimental data with Voigt profiles is shown by the orange line, and the individual Voigt peaks are shown in light blue. (b) Infrared spectra collected at selected pressures. Red (green) color indicates the low-pressure (LP) [high-pressure (HP)] phase. Pressures are indicated, the units for pressure are gigapascals, the up arrows at 9.6 GPa mark extra IR peaks, which are a sign of the phase transition. (c) Contour plot of the same data in (b); the horizontal dash line indicates the start of the phase transition.

TABLE V. Frequency (ω), pressure coefficient ($d\omega/dP$), and Grüneisen parameters (γ) for different IR-active modes of the LP (top) and HP (bottom) phase. More details can be found in the caption of Table III. The miss of the pressure coefficient and Grüneisen parameters for the experimental modes 156, 182, and 189 cm^{-1} is due to insufficient data at HP. The complete theoretical predicted modes for LP and HP phases can found in Tables S1 and S3 in Supplemental Material [36].

	Theory (at 0 GPa, $B_0 = 26.4$ GPa)			Experiment (at 0.7 GPa, $B_0 = 22.2$ GPa)		
Modes	ω (cm^{-1})	$d\omega/dP$ (cm^{-1}/GPa)	γ	ω (cm^{-1})	$d\omega/dP$ (cm^{-1}/GPa)	γ
B	135.69	5.46	1.06	139	7.84	1.25
B	142.20	2.98	0.55	156	×	×
A	155.07	5.01	0.85	172	7.22	0.93
A	163.35	5.63	0.91	182	×	×
A	172.45	9.10	1.39	189	×	×
A	184.56	9.89	1.41	198	6.56	0.74
B	211.11	10.62	1.33	222	9.72	0.97
B	220.82	9.24	1.10	238	5.96	0.56
B	242.47	7.45	0.81	259	9.39	0.80
B	324.99	4.70	0.38	329	2.20	0.15
A	342.87	5.53	0.43	353	5.05	0.32
A	364.69	4.66	0.34	380	4.39	0.26
A	409.35	8.92	0.58	408	2.22	0.12
A	416.32	8.89	0.56	429	1.25	0.06
	Theory (at 10.0 GPa, $B_0 = 44.4$ GPa)			Experiment (at 9.6 GPa, $B_0 = 63.6$ GPa)		
A	199.40	2.97	0.66	204	4.96	1.55
A	224.96	2.34	0.46	236	0.97	0.26
E	259.91	6.91	1.18	259	8.21	2.02
E	281.96	7.02	1.10	279	5.92	1.35
E	320.46	3.32	0.46	321	0.82	0.16
E	360.82	5.99	0.74	355	5.49	0.98
E	411.78	6.68	0.72	396	9.72	1.56
A	430.23	8.63	0.89	423	9.57	1.44
E	477.20	6.03	0.56	463	8.78	1.21

bonds finishes when the IO_6 unit becomes more regular, i.e., with almost a single I-O bond distance at ∼48 GPa by fitting the calculation data. From the Raman spectra collected after releasing pressure (Supplemental Material, Fig. S4 [36]), the phase transition is reversible, as found in HP-XRD.

C. HP-FTIR measurements

Figure 6(a) shows the FTIR spectra of $Mg(IO_3)_2$ at the lowest pressure (0.7 GPa) in the far-IR range (130–600 cm^{-1}). Table V summarizes the frequencies of the IR-active modes obtained from a peak fitting performed using Voigt profiles. The symmetry of the IR-active modes has been assigned based on calculations as done for the Raman-active modes. A total of 14 IR-active modes has been determined at 0.7 GPa. Since all optical modes of $Mg(IO_3)_2$ are both Raman and IR active, we will compare the results obtained from both techniques. However, it must be considered that usually strong modes in the Raman spectrum tend to be weak modes in the IR spectrum and vice versa. In the range of 300–500 cm^{-1}, where modes are related to I-O bending vibrations of $[IO_3]^-$ units, six Raman-active modes and five IR-active modes have been detected. Only two of them have been found at similar frequencies by both techniques. The Raman-active modes at 327 and 413 cm^{-1} were measured at 329 and 408 cm^{-1} in IR. The rest of the modes are not the same, so both techniques can complement to each other. Thanks to calculations, the IR-active mode at 353 cm^{-1} can be assigned to an asymmetric I-O bending of IO_3^- units, while the IR-active modes at 380 and 429 cm^{-1} can be assigned to the symmetric I-O bending of IO_3^- units. In addition, we found three IR-active modes at 222, 238, and 259 cm^{-1} but only one Raman mode in the range of 200–300 cm^{-1} (the mode at 238 cm^{-1}). Unfortunately, the 259 cm^{-1} mode cannot be followed at HP.

Figure 6(b) displays the evolution of the IR spectrum of $Mg(IO_3)_2$ under compression. The experimental cutoff frequency was 700 cm^{-1}. In Fig. 6(c), we show a contour plot of the same data. It can be observed that there are IR peaks appearing at wave numbers > 600 cm^{-1} in Figs. 6(b) and 6(c) beyond 6.6 GPa. These are stretching modes originally at frequencies > 700 cm^{-1} which soften under compression, as discussed in the Raman section. Remember that all modes in $Mg(IO_3)_2$ are both Raman and IR active. All IR-active modes in the medium-frequency range harden in the pressure range of stability of the LP and HP phases as it was found in Raman measurements. On the other hand, the IR-active modes of the high-frequency range soften at HP as it was found in Raman measurements. The pressure dependence of the frequencies of the IR-active modes is shown in Fig. 7.

The splitting of the IR peak at 250 cm^{-1} is due to the presence of two modes with a different pressure coefficient. In addition, there is a significant broadening and merging of the peaks in the 300–500 cm^{-1} range. The appearance of two new peaks at 9.6 GPa (with wave numbers 236 and 279 cm^{-1})

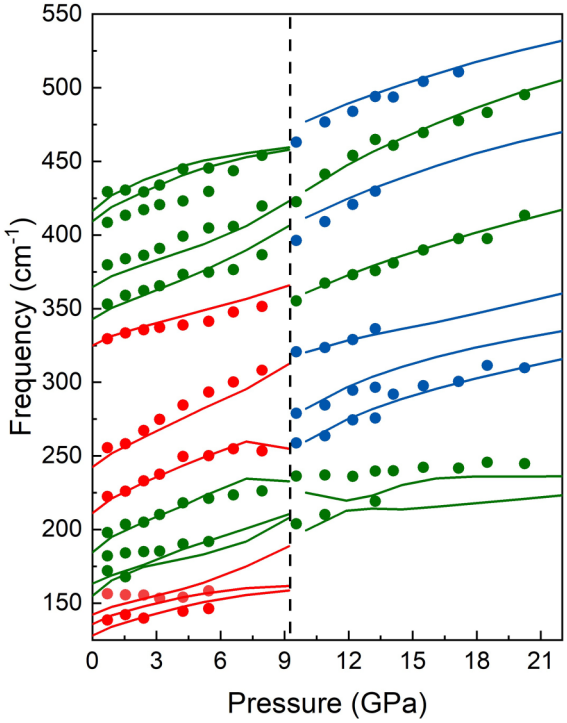

FIG. 7. Experimental (dots) and calculated (solid lines) determined infrared (IR) modes as a function of pressure. A, B, and E symmetry are shown in green, red, and blue, respectively. The symmetry of the experimentally observed IR modes has been assigned based on the same method used in the symmetry assignment of Raman modes; the vertical dashed line indicates the phase transition.

evidences the onset of the phase transition [see arrows in Fig. 6(b)]. The frequency of one of the extra peaks found in IR experiments is close to that of one of the extra peaks found in the Raman spectra at 9.4 GPa [which is shown in dark yellow in Fig. 4(a)]. A total of nine IR-active modes have been determined at 9.6 GPa. They are summarized in Table V (and Table S3 in the Supplemental Material [36]) together with the symmetry assignment. The nine modes will merge into four modes at pressures > 18 GPa. This result agrees with the expected merging of peaks at HP that will occur because of the equalization of the I-O bond distances in the IO_6 unit, i.e., upon the increase in symmetry of the IO_6 unit. All the pressure-induced changes in the IR spectra are reversible, as shown in Fig. 6(b).

IV. CONCLUSIONS

By combining the use of DACs, synchrotron-based angle dispersion powder XRD, RS, FTIR spectroscopy, and first-principle calculations, we discovered a pressure-induced phase transition and oxygen coordination increase (from 3 to 6) of iodine in metal iodate $Mg(IO_3)_2$. According to Rietveld refinements of HP-XRD data, $Mg(IO_3)_2$ transforms from the monoclinic LP phase (space $P2_1$) to a trigonal HP phase (space group $P3$) between 7.5 and 9.7 GPa. At the transition, the number of formula units per unit cell changes from 4 to 3: There is no obvious collapse in the volume per formula unit at the transition. The bulk modulus increases from 22.2 GPa (in the LP phase) to 63.6 GPa (in the HP phase) according to experiments. Additionally, the compressibility of the LP phase is highly anisotropy. The b axis is by far the most compressible. This is a result of the layered character of the crystal structure. Calculations revealed that pressure application leads to increase in the I-O bond length, which is accompanied by a shortening of the bond distance of iodine and second neighboring oxygen atoms. This favors a gradual increase of the oxygen coordination of iodine. This behavior is caused by the existence of LEP in iodine.

According to HP-RS and HP-FTIR experiments, the phase transition takes place between 7.7 and 9.6 GPa. The phase transition is evidenced by the appearance of extra peaks and the gradually enhancement of their intensity. The vibration symmetry of all experimentally observed Raman- and IR-active modes has been assigned by the comparison between experiments and calculations. In the LP phase, the vibrational modes in the midfrequency range (300–550 cm^{-1}) are related to I-O bending motions of $[IO_3]^-$ units, while those of the high-frequency range (600–900 cm^{-1}) are related to I-O stretching motions of $[IO_3]^-$ units. While the modes in the midfrequency range harden at HP, the modes at the high-frequency range soften at HP in both the LP and HP phases. This softening is caused by the increase of the I-O bond distances at HP and the charge transfer from short I-O bonds to large I-O bonds to form IO_6 units at HP. The phase transition found by the three experimental techniques was found to be reversible.

ACKNOWLEDGMENTS

This paper was supported by the Generalitat Valenciana under Project PROMETEO 2018/123-EFIMAT and by the Spanish Ministerio de Ciencia e Innovación and Agencia Estatal de Investigación (MCIN/AEI/10.13039/501100011033) and by the European Union under Grants PID2019-106383GB-41/42/43, and RED2018-102612-T (MALTA Consolider Team). A.M. and P.R.-H. acknowledge computing time provided by Red Española de Supercomputación (RES) and the MALTA Consolider Team cluster. D.E. acknowledges the resources and technical assistance provided by the Informatics Service of Universitat de Valencia through the Tirant III cluster. A.L. and D.E. would like to thank the Generalitat Valenciana for the Ph.D. Fellowship No. GRISOLIAP/2019/025. R.T. acknowledges funding from the Spanish Ministerio de Economía y Competitividad (MINECO) via the Juan de la Cierva Formación fellowship (FJC2018-036185-I). C.P. is thankful for the financial support of the Spanish Mineco Project No. FIS2017-83295-P. E.B. would like to thank the University of Valencia for his "Attracció de Talent" postdoctoral contract (UV-INV_POSTDOC19-1026935). Powder XRD experiments were performed at the MSPD beamline of ALBA Synchrotron (Experiment No. 2019083663). IR experiments were performed at the MIRAS beamline of ALBA Synchrotron (experiment No. 2020024118).

[1] H. Y. Chang, S. H. Kim, M. O. Kang, and P. S. Halasyamani, Polar or nonpolar? $A+$ cation polarity control in $A_2Ti(IO_3)_6$ (A = Li, Na, K, Rb, Cs, Tl), J. Am. Chem. Soc. **131**, 6865 (2009).

[2] H. Y. Chang, S. H. Kim, P. S. Halasyamani, and K. M. Ok, Alignment of lone pairs in a new polar material: synthesis, characterization, and functional properties of $Li_2Ti(IO_3)_6$, J. Am. Chem. Soc. **131**, 2426 (2009).

[3] C. F. Sun, C. L. Hu, X. Xu, J. B. Ling, T. Hu, F. Kong, X. F. Long, and J. G. Mao, $BaNbO(IO_3)_5$: a new polar material with a very large SHG response, J. Am. Chem. Soc. **131**, 9486 (2009).

[4] S. D. Nguyen, J. Yeon, S. H. Kim, and P. S. Halasyamani, $BiO(IO_3)$: a new polar iodate that exhibits an Aurivillius-type $(Bi_2O_2)^{2+}$ layer and a large SHG response, J. Am. Chem. Soc. **133**, 12422 (2011).

[5] X. Xu, C. Hu, B. Li, B. Yang, and J. Mao, α-AgI_3O_8 and β-AgI_3O_8 with large SHG responses: polymerization of IO_3 groups into the I_3O_8 polyiodate anion, Chem. Mater. **26**, 3219 (2014).

[6] Y. Huang, X. Meng, P. Gong, L. Yang, Z. Lin, X. Chen, and J. Qin, $A_2BiI_5O_{15}$ (A = K+ or Rb +): two new promising nonlinear optical materials containing $[I_3O_9]^{3-}$ bridging anionic groups, J. Mater. Chem. C **2**, 4057 (2014).

[7] L. Xiao, Z. Cao, J. Yao, Z. Lin, and Z. Hu, A new cerium iodate infrared nonlinear optical material with a large second-harmonic generation response, J. Mater. Chem. C **5**, 2130 (2017).

[8] F. F. Mao, C. L. Hu, J. Chen, B. L. Wu, and J. G. Mao, $HBa_{2.5}(IO_3)_6(I_2O_5)$ and $HBa(IO_3)(I_4O_{11})$: explorations of second-order nonlinear optical materials in the alkali-earth polyiodate system, Inorg. Chem. **58**, 3982 (2019).

[9] C. Sun, B. Yang, and J. Mao, Structures and properties of functional metal iodates, Sci. China Chem. **54**, 911 (2011).

[10] C. L. Hu and J. G. Mao, Recent advances on second-order NLO materials based on metal iodates, Coord. Chem. Rev. **288**, 1 (2015).

[11] D. Phanon and I. Gautier-Luneau, Promising material for infrared nonlinear optics: NaI_3O_8 salt containing an octaoxotriiodate(V) anion formed from condensation of $[IO_3]^-$ ions, Angew. Chem. Int. Ed. **46**, 8488 (2007).

[12] D. Phanon, A. Mosset, and I. Gautier-Luneau, New materials for infrared non-linear optics. Syntheses, structural characterisations, second harmonic generation and optical transparency of $M(IO_3)_3$ metallic iodates, J. Mater. Chem. **17**, 1123 (2007).

[13] R. Chikhaoui, Z. Hebboul, M. A. Fadla, K. Bredillet, A. Liang, D. Errandonea, S. Beauquis, A. Benghia, J. C. Marty, R. Le Dantec, Y. Mugnier, and E. Bandiello, Synthesis and characterization of novel nanoparticles of lithium aluminum iodate $LiAl(IO_3)_4$, and DFT calculations of the crystal structure and physical properties, Nanomaterials **11**, 3289 (2021).

[14] A. Liang, P. Rodríguez-Hernandez, A. Munoz, S. Raman, A. Segura, and D. Errandonea, Pressure-dependent modifications in the optical and electronic properties of $Fe(IO_3)_3$: the role of Fe $3d$ and I $5p$ lone-pair electrons, Inorg. Chem. Front. **8**, 4780 (2021).

[15] K. Bu, H. Luo, S. Guo, M. Li, D. Wang, H. Dong, Y. Ding, W. Yang, and X. Lü, Pressure-regulated dynamic stereochemical role of lone-pair electrons in layered Bi_2O_2S, J. Phys. Chem. Lett. **11**, 9702 (2020).

[16] A. Liang, C. Popescu, F. J. Manjon, A. Muñoz, Z. Hebboul, and D. Errandonea, Structural and vibrational study of $Zn(IO_3)_2$ combining high-pressure experiments and density-functional theory, Phys. Rev. B **103**, 054102 (2021).

[17] A. Liang, C. Popescu, F. J. Manjon, R. Turnbull, E. Bandiello, P. Rodriguez-Hernandez, A. Muñoz, I. Yousef, Z. Hebboul, and D. Errandonea, Pressure-driven symmetry-preserving phase transitions in $Co(IO_3)_2$, J. Phys. Chem. C **125**, 17448 (2021).

[18] A. Liang, S. Rahman, P. Rodriguez-Hernandez, A. Muñoz, F. J. Manjón, G. Nenert, and D. Errandonea, High-pressure Raman study of $Fe(IO_3)_3$: soft-mode behavior driven by coordination changes of iodine atoms, J. Phys. Chem. C **124**, 21329 (2020).

[19] A. Liang, S. Rahman, H. Saqib, P. Rodriguez-Hernandez, A. Munoz, G. Nenert, I. Yousef, C. Popescu, and D. Errandonea, First-order isostructural phase transition induced by high-pressure in $Fe(IO_3)_3$, J. Phys. Chem. C **124**, 8669 (2020).

[20] J.-K. Liang, Y.-D. Yu, and S.-L. Ding, The structure and phase transitions of magnesium iodate crystals, Acta Phys. Sin. **27**, 710 (1978).

[21] D. Phanon, B. Bentria, E. Jeanneau, D. Benbertal, A. Mosset, and I. Gautier-Luneau, Crystal structure of $M(IO_3)_2$ metal iodates, twinned by pseudo-merohedry, with M^{II}: Mg^{II}, Mn^{II}, Co^{II}, Ni^{II} and Zn^{II}, Z. Kristallogr. Cryst. Mater. **221**, 635 (2006).

[22] A. Dewaele, P. Loubeyre, and M. Mezouar, Equations of state of six metals above 94 GPa, Phys. Rev. B **70**, 094112 (2004).

[23] S. Klotz, J. C. Chervin, P. Munsch, and G. Le Marchand, Hydrostatic limits of 11 pressure transmitting media, J. Phys. D. Appl. Phys. **42**, 075413 (2009).

[24] F. Fauth, I. Peral, C. Popescu, and M. Knapp, The new material science powder diffraction beamline at ALBA Synchrotron, Powder Diffr. **28**, 360 (2013).

[25] C. Prescher and V. B. Prakapenka, DIOPTAS: a program for reduction of two-dimensional x-ray diffraction data and data exploration, High Press. Res. **35**, 223 (2015).

[26] J. Rodríguez-Carvajal, Recent advances in magnetic structure determination by neutron powder diffraction, Phys. B Condens. Matter **192**, 55 (1993).

[27] H. K. Mao, J. Xu, and P. M. Bell, Calibration of the ruby pressure gauge to 800 kbar under quasi-hydrostatic conditions, J. Geophys. Res. **91**, 4673 (1986).

[28] E. D. Palik, *Handbook of Optical Constants of Solid* (Academic Press, Maryland, 1997).

[29] D. Errandonea, A. Muñoz, and J. Gonzalez-Platas, Comment on "High-pressure x-ray diffraction study of YBO_3/Eu^{3+}, $GdBO_3$, and $EuBO_3$: Pressure-induced amorphization in $GdBO_3$" [J. Appl. Phys. **115**, 043507 (2014)], J. Appl. Phys. **115**, 216101 (2014).

[30] I. Yousef, L. Ribó, A. Crisol, I. Šics, G. Ellis, T. Ducic, M. Kreuzer, N. Benseny-Cases, M. Quispe, P. Dumas, S. Lefrançois, T. Moreno, G. García, S. Ferrer, J. Nicolas, and M. A. G. Aranda, MIRAS: the infrared synchrotron radiation deamline at ALBA, Synchrotron Radiat. News **30**, 4 (2017).

[31] A. Liang, R. Turnbull, E. Bandiello, I. Yousef, C. Popescu, Z. Hebboul, and D. Errandonea, High-pressure spectroscopy study of $Zn(IO_3)_2$ using far-infrared synchrotron radiation, Crystals **11**, 34 (2021).

[32] P. Hohenberg and W. Kohn, Inhomogeneous electron gas, Phys. Rev. **136**, B864 (1964).

[33] G. Kresse and J. Furthmüller, Efficient iterative schemes for *ab initio* total-energy calculations using a plane-wave basis set, Phys. Rev. B **54**, 11169 (1996).
[34] P. E. Blöchl, Projector augmented-wave method, Phys. Rev. B **50**, 17953 (1994).
[35] G. Kresse and D. Joubert, From ultrasoft pseudopotentials to the projector augmented-wave method, Phys. Rev. B **59**, 1758 (1999).
[36] See Supplemental Material at http://link.aps.org/supplemental/10.1103/PhysRevB.105.054105 for additional information on structural and vibrational analysis.
[37] H. J. Monkhorst and J. D. Pack, Special points for Brillouin-zone integrations, Phys. Rev. B **13**, 5188 (1976).
[38] R. Armiento and A. E. Mattsson, Functional designed to include surface effects in self-consistent density functional theory, Phys. Rev. B **72**, 085108 (2005).
[39] A. E. Mattsson, R. Armiento, J. Paier, G. Kresse, J. M. Wills, and T. R. Mattsson, The AM05 density functional applied to solids, J. Chem. Phys. **128**, 084714 (2008).
[40] A. Togo and I. Tanaka, First principles phonon calculations in materials science, Scr. Mater. **108**, 1 (2015).
[41] A. Krapp, F. M. Bickelhaupt, and G. Frenking, Orbital overlap and chemical bonding, Chem. Eur. J. **12**, 9196 (2006).
[42] F. D. Murnaghan, The compressibility of media under extreme pressures, Proc. Natl. Acad. Sci. USA **30**, 244 (1944).
[43] F. Birch, Finite elastic strain of cubic crystals, Phys. Rev. **71**, 809 (1947).
[44] R. J. Angel, J. Gonzalez-Platas, and M. Alvaro, EOSFIT7C and a Fortran module (library) for equation of state calculations, Z. Kristallogr. Cryst. Mater. **229**, 405 (2014).
[45] L. Bayarjargal, L. Wiehl, A. Friedrich, B. Winkler, E. A. Juarez-Arellano, W. Morgenroth, and E. Haussühl, Phase transitions in KIO_3, J. Phys. Condens. Matter **24**, 325401 (2012).
[46] W. W. Zhang, Q. L. Cui, Y. W. Pan, S. S. Dong, J. Liu, and G. T. Zou, High-pressure x-ray diffraction study of $LiIO_3$ to 75 GPa, J. Phys. Condens. Matter **14**, 10579 (2002).
[47] A. Lobato, M. A. Salvadó, J. M. Recio, M. Taravillo, and V. G. Baonza, Highs and lows of cond lengths: is there any limit? Angew. Chem. Int. Ed. **60**, 17028 (2021).
[48] Z. X. Shen, X. B. Wang, S. H. Tang, H. P. Li, and F. Zhou, High pressure Raman study and phase transitions of KIO_3 non-linear optical single crystals, Rev. High Press. Sci. Technol. **7**, 751 (1998).
[49] T. C. Kochuthresia, I. Gautier-Luneau, V. K. Vaidyan, and M. J. Bushiri, Raman and FTIR spectral investigations of twinned $M(IO_3)_2$ (M = Mn, Ni, Co, and D Zn) crystals, J. Appl. Spectrosc. **82**, 941 (2016).
[50] K. Momma and F. Izumi, VESTA 3 for three-dimensional visualization of crystal, volumetric and morphology data, J. Appl. Crystallogr. **44**, 1272 (2011).